ELSEVIER

Contents lists available at ScienceDirect

Journal of Manufacturing Processes

journal homepage: www.elsevier.com/locate/manpro





Rapid forming of high-entropy alloy under extreme low temperature via ultrasonic vibration

Yu Zhang ^{a,b}, Pengyu Huang ^b, Luyao Li ^b, Xin Li ^b, Wenxin Wen ^b, Sajad Sohrabi ^b, Jinbiao Huang ^b, Wenhao Lu ^b, Yong Xiao ^{a,*}, Dan Li ^a, Jiang Ma ^{b,*}

- ^a School of Materials Science and Engineering, Wuhan University of Technology, Wuhan 430070, China
- ^b Shenzhen Key Laboratory of High Performance Nontraditional Manufacturing, College of Mechatronics and Control Engineering, Shenzhen University, Shenzhen 518060. China

ARTICLE INFO

Keywords: Ultrasonic vibration High-entropy alloy Low temperature Plastic deformation

ABSTRACT

Low-temperature forming technology has a wide range of applications, particularly in aerospace and polar exploration. However, its application often confined by the low-temperature brittleness of metallic materials. This study proposes a simple and efficient route to form high-entropy alloys at a low temperature (77 K) using ultrasonic vibration, termed ultrasonic-assisted plastic forming. Our findings demonstrate that this ultra-fast processing technology can achieves a macroscopic high strain rate of $1.25 \times 10^{-1} \, \rm s^{-1}$ with significantly lower stress compared to conventional compression methods. The reduction in stress is attributed to the deformation twin and large angle grain rotation induced by ultrasonic vibration, which activate additional slip systems and facilitates deformation. The Vickers hardness in the processed surface increases by 39.1 % compared to the ascast sample, suggesting the method enables simultaneous surface modification and forming. Furthermore, fine multi-scale structures and with small parts of special shapes are fabricated successfully using the proposed method. The detailed structure characterization of the formed sample and the proposed forming mechanism provide valuable insight into deformation under dynamic loading. Owing to its high efficiency and lightweight equipment requirements resulting from low forming stress, ultrasonic-assisted plastic forming holds potential for engineering applications in forming metal alloys, even in extreme environments.

1. Introduction

The manufacturing of alloys in extreme environments is a critical aspect of developing industrial capabilities [1]. Li et al. [2] proposed that a low ambient temperatures, specifically those below ~220 K can be identified an extreme environment for industrial production. Numerous scientific research and exploration projects are conducted under such low temperatures, such as space exploration [3], superconducting devices [4], lunar missions [5], polar expeditions [6], and deep-sea explorations [7]. These projects all need to withstand the challenge of environmental temperatures tens of degrees below freezing. Williams et al.[8] reported that the average minimum temperature in the polar region of the moon can even reach approximately 20 K. Panin et al.[9] have reported that low temperatures can increase the brittleness of materials making them more prone to failure. Additionally, thermal expansion and contraction can cause alterations in structural components and dimensions [10], leading to reduced material flexibility

and increasing the difficulty of manufacturing processes [11]. Consequently, these challenges necessitate the development of advanced manufacturing techniques and materials tailored to withstand extreme low-temperature environments.

Researchers have made significant efforts and achieved breakthroughs in developing alloys with excellent mechanical properties through methods such as friction stir processing [12], preparation of ultra-fine-grain [13], and achieving superplasticity even at low temperatures [14]. As an emerging material, the performance of highentropy alloys (HEAs) performs particularly well in low-temperature environments. For instance, Otto et al. [15] reported that the equiatomic CoCrFeNiMn HEA exhibits a 50 % increase in strength and a 30 % increase in ductility at a low temperature of 77 K. This improvement is attributed to the formation of nanoscale twins after reaching a strain of 20 % or more, which enhances the work hardening rate and allows for higher ductility. Similarly, Muhammad Naeem et al. [16] reported that the yield and tensile strength of CrFeCoNi HEA increased by 100 %,

E-mail addresses: yongxiao@whut.edu.cn (Y. Xiao), majiang@szu.edu.cn (J. Ma).

^{*} Corresponding authors.

accompanied by a significant increase in flexibility (from 45 % to 58.4 %) as the temperature decreased from room temperature (RT) to 25 K. The fractured sample at 25 K exhibited minimal necking, supporting a notable uniform elongation.

Despite these advancements, most research has focused on the tensile properties of HEAs, with strain rates typically in the order of magnitude of 10^{-4} s⁻¹ to 10^{-5} s⁻¹ [17]. The Exploration of deformation at high strain rates and forming components via compression at low temperatures is meaningful but remains relatively understudied but holds significant potential. In previous works, ultrasonic vibration (UV) has been identified as a highly effective strategy for the forming process of HEAs [18], forming bulk metallic glasses in a liquid environment [19], rejuvenating aged bulk metallic glasses [20], and joining two MGs into a bigger one [21], even in the liquid environment [22]. By applying 20 kHz UV and a stress of 100 MPa (only 1/6 of compression strength), the compression strain of the Al₈₀Li₅Mg₅Zn₅Cu₅ HEA surges from the conventional 17 % to a remarkable 30 % within 1-3 s [23]. Ultrasonic vibration-assisted plastic forming (UAPF) has also been confirmed to be a useful strategy for forming multi-scale structures on CoCrFeNiMn HEA in milliseconds [24], showing that UV can enhance the material's plastic deformation capability while achieving the forming process.

Low-temperature forming poses challenges in terms of the materials themselves and the processing tools. The fast energy release speed of UV can ensure high efficiency, while the low processing stress can reduce power consumption, and the equipment volume is also lower than conventional forming machinery, making it more suitable for industrial production. In this context, UV can be a potential forming process worth studying.

In this work, we explored UAPF under extremely low ambient temperatures during UAPF. The entire experiment was conducted in a continuous liquid nitrogen environment. During the process, cylindrical samples with a height of 3 mm could be strained by 50 % in 3–4 s, which demonstrates its high efficiency. The processed surface showed a 39.1 % increase in hardness caused by grain refinement, indicating that UAPF enables surface modification while forming. The observation of twins in the micro-structure of the UAPF sample, which was absent in the conventionally compressed sample, revealed that UAPF has the potential to reach higher plastic deformation. In addition, the presence of twins, along with the observed angle of grain rotation, can help initiate more slip systems, reducing the required stress for UAPF compared to static conventional compression. Using this approach, we successfully fabricated multi-scale structures and small parts of special shapes.

This work highlights that the proposed UAPF method can efficiently form materials with low machining stress. Combined with the superior performance of Cantor alloy at low temperatures, this method may have potential engineering applications in aerospace and polar exploration, where a low-temperature manufacturing environment is essential. The detailed structural characterization and deformation mechanism under UV in this study can also provide references for the deformation research of alloys under high-frequency dynamic loading.

2. Materials and methods

2.1. Sample preparation

The equiatomic CoCrFeNiMn HEA was prepared by vacuum-induction melting. Each raw material of the elements had a purity of 99.99 % by weight. Samples with a diameter of 3 mm and a length of 3 mm were cut from the prepared ingot by using wire electrical discharge machining-low speed (WEDM-LS, a-C400, FANUC, Japan). The external surfaces of each sample were polished with sandpapers of 500, 1000, and 2000 grit to remove oxide films and ensure that the top and bottom sides were parallel.

2.2. Low-temperature environment and temperature measurements

To create a low-temperature environment, a glass container filled with liquid nitrogen was used throughout the entire experiment. To investigate the impact of rising temperatures during the experiment, a thin gauge thermocouple wire equipped with a sampling frequency of 1000 Hz data acquisition system (TD-3304C, KAIAN, China) was used to measure temperature variations during the process.

2.3. Processing stress measurements

The sample was placed on a dynamometer (QLMH, QILI, China) to remeasure the real-time force during UAPF. The dynamometer has threaded holes on its surface to secure the UAPF mold. A data-acquisition card (National Instruments NI-9237) with a sampling frequency of 1000 Hz was used to collect and process the force data. The data was then transmitted to a computer through a data collection box (cDAQ-9174, NI, USA).

2.4. Conventional compression tests

A universal testing machine (UTM5305H, SANSI, China) was used to conduct conventional compression (CC) experiments. The compression test was performed in an environment of continuous liquid nitrogen refrigeration at 77 K using a strain rate of $1.25\times10^{-1}~\mbox{s}^{-1}$. The tested samples had a height of 3 mm and a diameter of 3 mm. The formed involute gears were also prepared with the mentioned machine.

2.5. Mold for forming

To verify the forming ability at low temperatures, anodic aluminum oxide (AAO) templates with nano-scale holes approximately 290 nm in diameter and 304 stainless steel molds with cross-groove structure (120 μm in width) were used to fabricate micro/nanostructures on the surface of the HEA. Furthermore, several molds with different shapes were designed for the experiment. The molds had a diameter of 10 mm and a thickness of 3 mm (see Fig. S1). The shapes included an involute gear, pentacle, square, and the alphabet "SZU", representing the abbreviation of Shenzhen University.

2.6. Preparation of involute gear

To compare the quality of formed parts by CC and UAPF, a cylindrical HEA was placed on the mentioned involute gear mold. After these two kinds of compression, the HEA underwent plastic deformation and was squeezed into the mold, resulting in the designed gear shape.

2.7. Surface mechanical properties tests

Mechanical properties from the sample cross-section were tested using a nanoindentation apparatus (TI 980, Bruker, Germany) equipped with a Berkovich tip, applying a maximum loading rate of $0.5 \text{mNs}^{-1}.$ The hardness and elastic modulus variations at 0.1 mm depth intervals, in conventional compressed and UAPF samples were tested on the cross-sectional plane, with each depth measurement repeated at least five times (interval 1 $\mu\text{m})$ to obtain an averaged value. Additionally, the surface hardness of all samples was measured using an automatic Vickers hardness tester (HM-210, MITUTOYO, Japan) at a load of 500 gf (4.90 N) for 10 s, with 100 points tested in a 1 mm \times 1 mm square.

2.8. Structure characterization

The morphology of involute gears formed by these two methods and the morphology of compressed samples were obtained by scanning electron microscopy (SEM; Quanta FEG 450, FEI, UAS), and their surface roughness was measured by atomic force microscopy (AFM; Cypher S, UK). All HEA thin film TEM samples were fabricated by SEM/focused ion beam (FIB) double beam system (FEI SCIOS, FEI, USA). Microstructure characteristics were tested through transmission electron microscopy (TEM; Titan Cubed Themis G2 300, FEI, USA), high-angle annular dark field (HAADF) imaging, and selected area electron diffraction (SEAD) patterns.

2.9. Electron backscatter diffraction

The electron backscattered diffraction (EBSD; OXFORD Nordlys-Max3, UK) technique was employed to analyze the microstructure changes in the deformation regions of the samples. The EBSD analysis was conducted using the TESCAN MAIA3 scanning electron microscope, which was equipped with an HKL-EBSD system. Before the test, the samples underwent ion-beam polishing for 2 h at 6.5 kV. During the EBSD characterizations, a step size of 1 μm was used, and the analysis was performed at an acceleration voltage of 20 kV. AZtecCrystal software was used to analyze the obtained data to get the grain distribution maps, local misorientation, and grain orientation spread maps.

2.10. Ultrasonic vibration setup

The ultrasonic vibration device used in this experiment was custommade (physical picture shown in Fig. S2), so no accurate model can be provided. Apart from adding testing equipment for some additional experimental parameters (such as temperature, and stress mentioned above) for experimental convenience, it is nearly identical to commercial production models. As demonstrated in Fig. 1a, it consists of 6 main components: the pneumatic system, control system, power supply, transducer, booster, and horn. The transducer, made of piezoelectric materials, converts electrical energy to mechanical vibrations. The booster amplifies vibration amplitude up to 44 μm , and the horn transfers the amplified mechanical vibration to the HEA sample. The force between the sample and the horn is provided by a pneumatic system, where the high-pressure gas stored in the air pump converts air pressure to mechanical pressure through a pneumatic piston. In addition to the mechanical hardware unit, a control system accurately controls the applied pressure, ultrasonic amplitude, and ultrasonic energy. For better data presentation, a coordinate system as shown in Fig. 1b was defined, with the direction of downward compression labeled as RD.

3. Results and discussion

3.1. Parameter monitoring during the UAPF process

As shown in Fig. 2a, HEA samples were immersed in a liquid nitrogen environment throughout the entire experimental process by designing a glass container on the processing substrate. The horn was in direct contact with the samples, transmitting pressure and 20 kHz ultrasonic vibration to achieve UAPF. During the process, the preset pressure of the horn driven by the pneumatic system is 400 kPa, and the amplitude is preset as 44 µm. The input energy was the only independent variable, adjusted by the control system. The detailed processing parameters are shown in Table 1, and the processed samples are shown in Fig. 2b. The strains corresponding to the energies of 100 J, 300 J, 500 J, 1000 J, and 2000 J were 16 %, 26 %, 35 %, 36 %, and 48 %, respectively. The variable strain shows a positive correlation with the applied energy, indicating that the strain can be effectively controlled by adjusting the input energy.

As seen in the inset of Fig. 2b, due to the concentration of ultrasonic energy near the surface, the near-surface region in contact with the horn underwent more plastic deformation. The sample extended in the direction perpendicular to the stress, which can improve the material's ability to fill the mold, thus being beneficial for forming. In contrast, the CC sample is uniformly thickened due to undergoing static uniaxial compression (see Fig. S3).

During the mechanical machining process, a certain level of thermal influence is inevitable due to friction. Therefore, temperature variations between the horn and the sample surface were measured and are shown in Fig. 2c. At the beginning and end of the process, the liquid nitrogen vapor continuously absorbed environmental heat as it evaporated, keeping the temperature constant at approximately 77 K [25]. However, temperature changes occurred due to friction between the horn and the samples in the process. The corresponding maximum temperature increases for input energies of 100 J, 500 J, and 2000 J were 200 K, 290 K, and 461 K, respectively. Owen et al.[26] reported that the melting point of CoCrFeNiMn HEA is approximately 1543 K, with no phase transition occurring before reaching this temperature. Therefore, the thermal effects generated during UV can be ignored, suggesting that deformation mainly relies on vibration and force. Consequently, the entire process can be considered as a cold heading process. However, one of the limiting factors in cold heading processes is the required high processing stress [27].

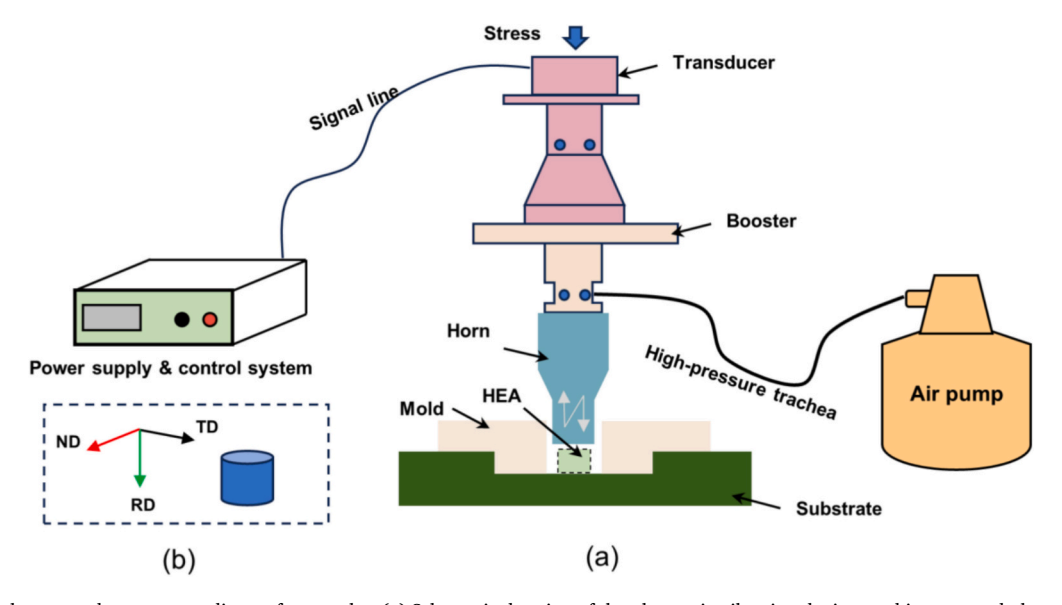


Fig. 1. Experimental setup and custom coordinates for samples. (a) Schematic drawing of the ultrasonic vibration device used in proposed ultrasonic-assisted plastic forming. (b) Customized sample coordinate system.

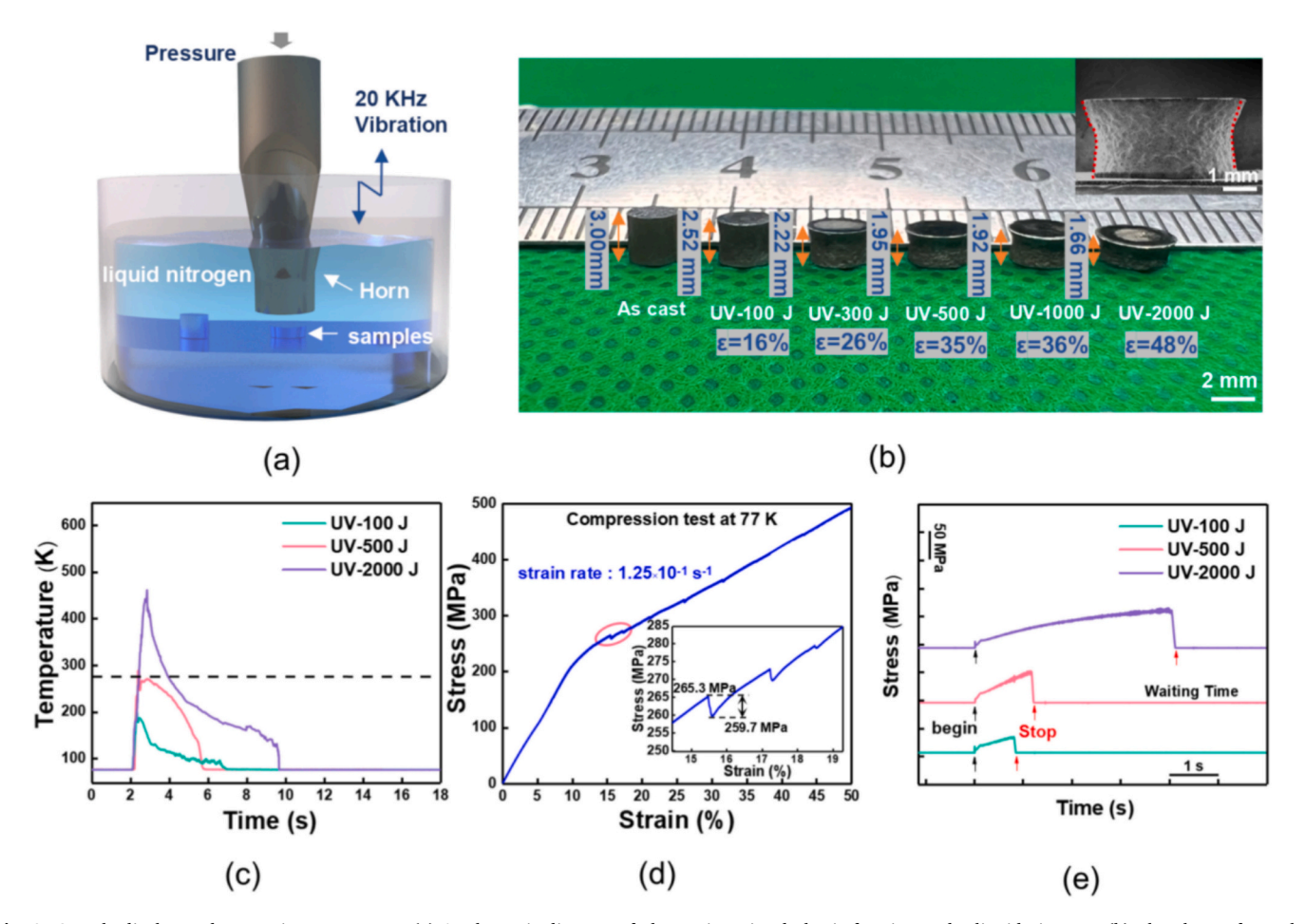


Fig. 2. Sample display and processing parameters. (a) A schematic diagram of ultrasonic-assisted plastic forming under liquid nitrogen. (b) The photo of samples processed under different input energies, the inset shows sample characteristics after ultrasonic-assisted plastic forming. (c) The temperature variation of the sample's contact surface with the horn throughout the entire processing process. (d) The stress-strain curve was conducted in conventional compression at 77 K with the same strain rate as in ultrasonic-assisted plastic forming, and the inset shows the Portevin-Le Chatelier (PLC) phenomenon during the yielding stage. (e) Mechanical response of samples under ultrasonic-assisted plastic forming.

Table 1Processing parameters of ultrasonic-assisted plastic forming.

	Energy (J)	Amplitude (μm)	Process time (s)
UV-100	100	44	0.9
UV-300	300	44	1.1
UV-500	500	44	1.6
UV-1000	1000	44	2.3
UV-2000	2000	44	4.1

To evaluate the difference in required stress between UAPF and CC, Fig. 2d shows a conventional compression curve at a strain rate of $1.25\times10^{-1}~\rm s^{-1}$. The strain rate was kept in the same order of magnitude as UAPF. As strain increased, work hardening occurred during the compression process, and the required stress gradually increased, reaching 264 MPa, 390 MPa, and 480 MPa when the strain was 16 %, 35 %, and 48 %, respectively. However, as shown in Fig. 2e, the stresses required for UAPF were 28 MPa, 54 MPa, and 70 MPa when reaching 16 %, 35 %, and 48 % strain, respectively. In comparison, the required stresses for UAPF to achieve the same three strains were 10.6 %, 13.8 %, and 14.6 % of conventional compression, respectively. This suggests that UV can effectively reduce the required stress for compression deformation.

Additionally, the Portevin-Le Chatelier (PLC) phenomenon [28] happened during the high strain rate conventional compression; a stress-serrated waveform can be observed in the inset of Fig. 2d, with a

fluctuation amplitude of approximately 5 MPa. This phenomenon provides evidence for the existence of strain localization, which increases the occurrence of localized plastic deformation in the material and affects its formability [29].

3.2. Surface quality of parts processed by CC and UAPF

Using identical molds, the same strain rates, and the same liquid nitrogen processing environments, two involute gears were prepared by CC and UAPF. As shown in Fig. 3a, striped streaks indicated by arrows have appeared on the surface of the sample, confirming that the PLC phenomenon occurred during CC forming. These defects caused by stress concentrations decrease the surface quality and usability of the sample [30], but defects are not obvious in the UAPF sample, because under high-frequency dynamic loading, the dislocation density and stress state will be more uniform compared to uniaxial static loading.

There is also a distinction in the replication ratio of processed samples. The size of the tooth tip structure of the gear is only a few hundred micrometers, so the intricate structure is difficult to plastically fill. When connecting lines separately, as shown in Fig. 3c along the tooth crest and tooth surface, two yellow lines formed an obtuse angle which indicates that the sample has not been fully replicated and formed a conical shape. In contrast, the same two lines formed in the sample processed by UAPF, as shown in Fig. 3d, have a right angle, indicating that a complete gear has been fully replicated. The details of the involute were also well-preserved, denoting that UAPF can achieve a higher replication ratio

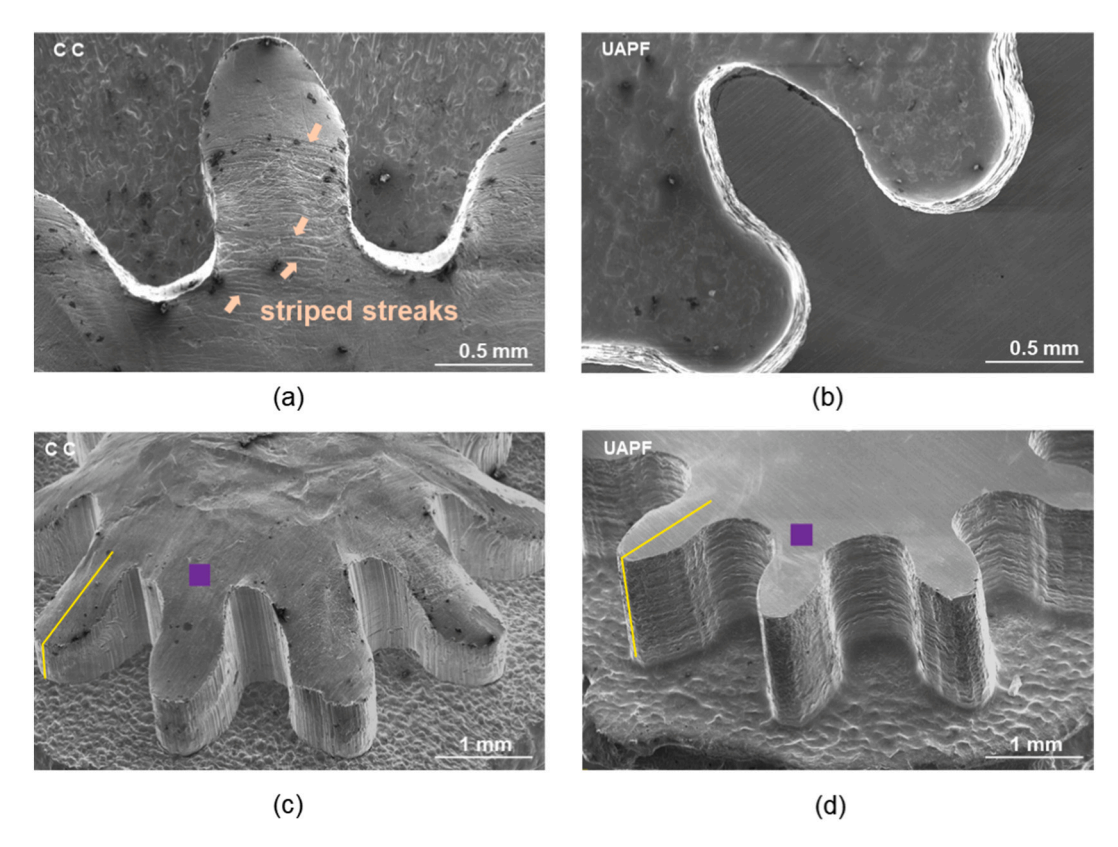


Fig. 3. Morphology of parts prepared by convention compression and ultrasonic-assisted plastic forming. (a) Scanning electron microscope (SEM) image of the surface of the involute gear processed by conventional compression. (b) SEM image of the surface of the involute gear processed by ultrasonic-assisted plastic forming. (C) A side view provides an overall SEM image of the involute gear processed by conventional compression forming. (d) A side view provides an overall SEM image of the involute gear processed by ultrasonic-assisted plastic forming, the purple box area is the sampling area for the next roughness test. (For interpretation of the references to color in this figure legend, the reader is referred to the web version of this article.)

in forming.

While the morphological surface quality of parts processed by CC and UAPF can be evaluated from the SEM images, a quantitative characterization of surface roughness was also carried out. The same region of processed involute gear, indicated by the purple square in Fig. 3c, d, was tested. The square is a 30 \times 30 μ m² region. Fig. 4a, b show the threedimensional surface regions from CC and UAPF samples respectively. Notably, the maximum and minimum values of the color bar were kept the same. In this case, the UAPF surface looks smoother because the undulations in its morphology are visually much smaller. For quantitative analysis, the average roughness value of the CC sample is 214 nm, while the average roughness value of UAPF is 63 nm. For a more intuitive presentation, Fig. 4c shows the depth variation along the red and blue lines. The undulation height and width of the CC sample are both larger, with the maximum height of the protrusion reaching 468 nm and the width of the protrusion reaching 15 µm. Through quantitative analysis, it has been found that the UAPF sample has a smoother surface. This benefit is attributed to the ultrasonic vibration surface effect, where the surface of sample and horn high-frequency dynamic contact, improves the friction relationship between the processed material with the mold and horn. This effect enhances the surface quality of the material, achieving the goals of improved forming efficiency and surface quality [31].

3.3. Mechanical properties of samples obtained by CC and UAPF

After discussing the differences in sample morphology, mechanical performance is also crucial as it determines the material's performance, service life, and usage scenarios [32]. For a better comparison between the HEAs obtained by CC and UAPF, the CC sample was subjected to the

same strain of 48 % as the sample obtained by UV. The inset in Fig. 5a shows a schematic illustration of the tested area, with nanoindentation tested along the RD direction at the red points, averaging 5 measurements every 0.1 mm in depth. Due to the slow uniaxial static loading of CC, the sample undergoes uniform plastic deformation, and the hardness value remains almost unchanged from top to bottom, fluctuating around 4.5 GPa. In comparison, in the UV-treated sample, as shown in Fig. 5b, a significant increase in hardness can be observed in the area close to the surface, with the maximum value reaching 5.1 GPa, which is 13.4 % higher than the CC sample. As the depth increases, the hardness gradually decreases and fluctuates around 4.5 GPa. Therefore, the sample processed by UV shows better mechanical performance on the near-surface than CC.

Although UV processing involves uniaxial stress, its dynamic loading manifests as sinusoidal vibrations at high frequencies. This can also be understood as a form of hammering. As shown in Fig. 5c, grain refinement is evident to a depth of more than 100 μm from the surface of HEA treated with 2000 J energy of UV. The increase in surface hardness of HEA obtained by UV is primarily due strengthening effect of grain boundaries [33].

In addition to grain refinement near the surface, the grain shape of the entire sample undergoes a certain degree of change to accommodate slip deformation. Fig. 6(a)–(d) corresponds to the grain distribution maps of the as-cast, UV-500, UV-2000, and CC samples, respectively. The red lines depict large-angle grain boundaries with an orientation difference higher than 10° , and the green line represents small-angle grain boundaries with an orientation difference of 2– 10° . The sampling location is the cross-section near the surface. Fig. 6a shows a grain distribution map of the as-cast sample, presenting the original grain shape with an average size of approximately 74.3 μ m. Fig. 6b shows the

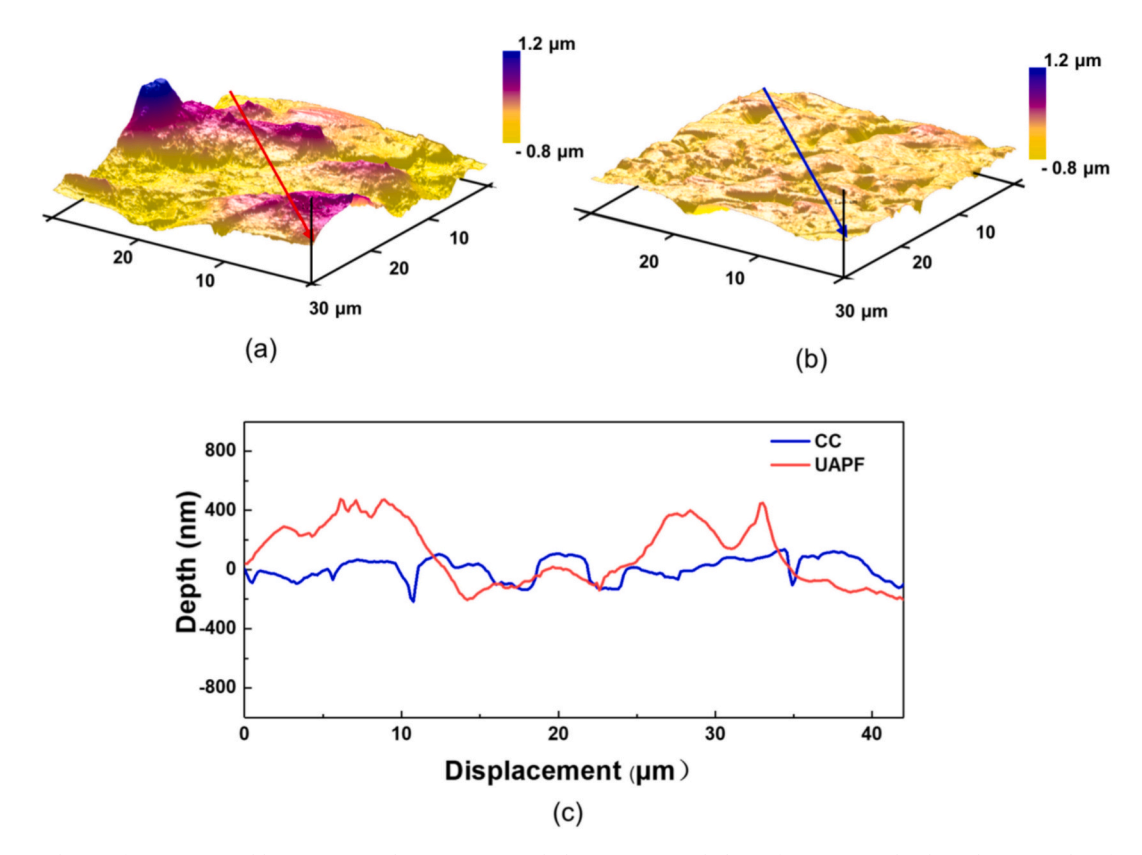


Fig. 4. Surface roughness of parts prepared by conventional compression and ultrasonic-assisted plastic forming. (a) The three-dimensional surface morphology in the purple area of Fig. 3c, the color scales represent the height of morphology, and the red line indicates the traces where the depth profile was taken. (b) The three-dimensional surface morphology in the purple area of Fig. 3d, the blue line indicates the traces where the depth profile was taken. (c) The depth variation along the red and blue lines. (For interpretation of the references to color in this figure legend, the reader is referred to the web version of this article.)

grain distribution map of the UV-500 J sample J, it is clear that grains underwent compression deformation along the direction of RD, and the original coarse grains formed sub-grains during UV, resulting in a reduction in the average grain size to 41.1 μm . Furthermore, as shown in Fig. 6c, the grains are flattened along the compression direction and elongated by squeezing in the perpendicular compression direction [34]. The average grain size has reduced by 55 % compared to the ascast sample, reaching 33.5 μm . On the other hand, the CC sample shown in Fig. 6d has a similar size as UV-2000, which is why their cross-sectional hardness fluctuates around 4.5 GPa, but the grain shape seems more scattered in CC.

Apart from the comparison of cross-sectional mechanical properties, the surface mechanical properties will determine the quality of the formed part. The hardness maps tested in a $1\times 1~\mathrm{mm}^2$ region are shown in Fig. 6e–h for each sample. The average hardness of the as-cast, UV-500, and UV-2000 are 184.4 HV, 244.1 HV, and 256.5 HV, respectively, with a maximum hardness increase of approximately 39.1 %, showing a positive correlation with the input energy. However, the average hardness of the CC sample is 220 HV. The hardness values between different positions are similar, and the accumulation of dislocations caused by deformation makes it higher than the as-cast, but lower than the UV sample due to the absence of surface grain refinement in CC samples.

3.4. High-resolution microstructural characterizations

As mentioned above, UAPF shows higher surface quality, higher replication ratio, significant improvement in mechanical performance, and much lower forming stress. To reveal the reasons behind these differences, a microscopic structural analysis between these two different compression methods was conducted. Fig. 7a shows a bright-field TEM image of the as-cast sample, displaying a crystal region with

no visible defects and dislocations. Corresponding elemental distribution maps are shown in Fig. 7b, where all five elements are uniformly distributed without any indications of segregation. A selected area electron diffraction (SAED) pattern from the as-cast sample was shown in Fig. 7c, with the pattern indexed to a face-centered cubic (FCC) structure along the $[\overline{1}\ \overline{1}0]$ zone axis.

For comparison, a bright-field TEM image after CC with a strain of 48 % is shown in Fig. 7d. The sampling location was from a processed surface, and obvious stacking faults (SFs) were observed. Enlarging one SF, as shown in Fig. 7e, reveals a surface defect generated due to a change in the stacking order of atoms. In addition to these surface defects, Fig. 7f exhibits the one-dimensional Fourier-filtered image of Fig. 7e, with the spots indicated in the inset of Fig. 7e in blue. Dislocations, marked by a symbol \perp in Fig. 7f, show the line defect. Additionally, apart from SFs observed in the UAPF sample with a strain of 48 %, some deformation twins (DTs) were observed in Fig. 7g. Enlarging one DT, as shown in Fig. 7h, reveals that the atom structures of DTs are different from SFs, with approximately 8 atoms on both sides of the dashed line being mirror-symmetric with respect to the dashed mirror plane. Fig. 7i shows a fast Fourier transform (FFT) image of Fig. 7h, it is two sets of identical single crystal spots, which have deviated by a certain angle, that is the same crystal that deflects a certain angle to form twin plans, further confirming the DT structure.

It is well recognized that CoCrFeNiMn HEA has an FCC structure, and the primary mechanisms of plastic deformation are slip and twin [35], with slip being the main method. Slip initiates from the densely packed atomic plane because it requires the least energy. The TEM micrographs of SFs and DTs all present at a 45° angle, which is precisely the location of the densely packed (1 1 1) plane. The deformation mode under CC and UAPF is dislocation-based because SFs can be observed by both these two methods. During compression, dislocation numbers increase

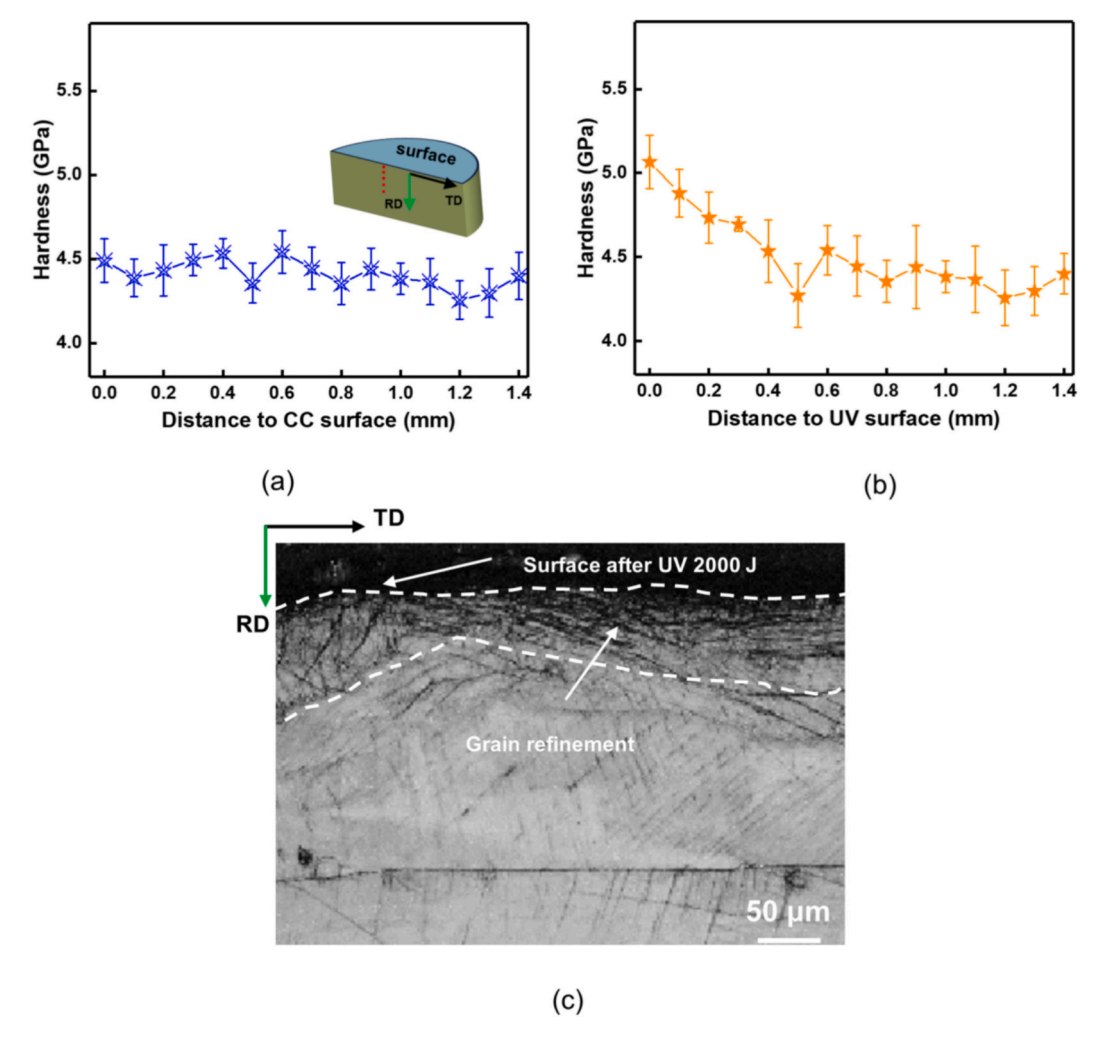


Fig. 5. Mechanical performance of sample prepared by conventional compression and ultrasonic-assisted plastic forming. (a) Nanoindentation hardness variation along RD in the high-entropy alloy (HEA) obtained by conventional compression, the error bars represent standard deviation from the mean value (n = 5), and the inset is a schematic illustration displaying the testing region. (b) Nanoindentation hardness variation along RD in HEA obtained by ultrasonic energy 2000 J. (c) the inset is the grain distribution on the cross-section of the HEA obtained by ultrasonic vibration.

rapidly, leading to dislocation entanglement [24], which makes further plastic deformation difficult. As previously mentioned, slip can only occur on specific crystal planes, but DT can alter crystal orientation, transforming certain challenging slip systems into more accessible ones [36]. Although both CC and UAPF are plastic deformation methods dominated by dislocations, UAPF benefits from the activation of new slip systems, facilitating multiple dislocation slips, which may enable a greater degree of plastic deformation.

3.5. Crystallographic analysis

To investigate the underlying mechanism for much lower forming stress for UAPF. Fig. 8 shows a detailed EBSD characterization. The local misorientation of grains is employed to assess the dislocation distribution after compression, and the densities of geometrically necessary dislocations (GND) can be calculated using the formula $\rho GND=2KAM_{ave}/\mu b$, where μ is the selected step size in EBSD experiments, b is the length of the Burgers vector, and KAM_{ave} represents the average KAM value for the selected region [37]. Geometric dislocation density is positively correlated with local misorientation. It should be noted that both samples were compressed with a strain of 48 % by CC and UAPF, the shooting positions for EBSD maps were the same position near the top surface.

Fig. 8(a) and (b) show the distribution of local misorientation of HEA

compressed by CC and UAPF, respectively. There are three color distributions in the map: blue, cyan, and yellow, representing angles of misorientation of $0-1.3^{\circ}$, $1.3-2.7^{\circ}$, and $2.7-4.0^{\circ}$, respectively. The inset of Fig. 8a shows the percentage of different colors in the map, with the misorientation angles of $0-1.3^{\circ}$, $1.3-2.7^{\circ}$, and $2.7-4.0^{\circ}$ being 27.7 %, 55 %, and 17.3 %, respectively, for the CC sample. The inset of Fig. 8b shows the percentage of different colors in the map, with the misorientation angles of 0-1.3°, 1.3-2.7°, and 2.7-4.0° being 47.4 %, 46.8 %, and 5.8 % in the UAPF sample. The CC sample exhibits more pronounced dislocation stacking. The black lines represent grain boundaries indicating that the orientation difference between two grains is larger than 10°. It has been discussed previously that slip is the primary deformation mechanism by CoCrFeNiMn HEA. When there is a certain orientation difference between grains, dislocations will be unable to continue propagating, leading to their accumulation at the edges where orientation differences occur. Thus, the yellow color representing high dislocation density mostly occurs along the black grain boundaries in Fig. 8a, b. This phenomenon is much more obvious in Fig. 8b, while some yellow color also appears inside the grain, as shown in Fig. 8a. The accumulation of dislocations within the crystal is due to excessive build-up of dislocations during uniaxial static compression, making it difficult to achieve proper release.

Fig. 8c, d show the grain orientation spread maps after CC and UAPF respectively. There are five color distributions in the map: blue, green,

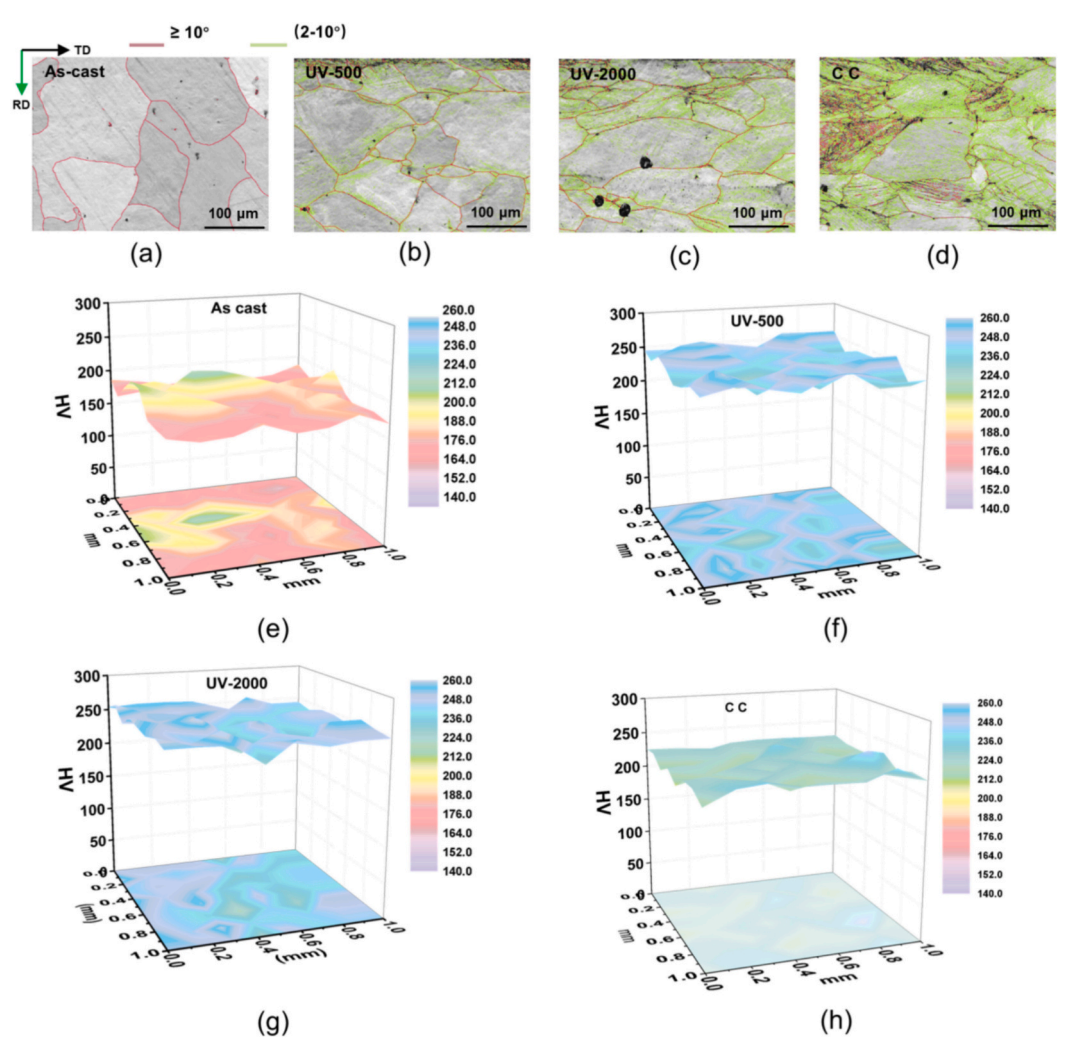


Fig. 6. Crystal structure and surface mechanical properties. (a)–(d) The grain distribution maps belonging to the cross-section near the compression contact surface of the as-cast, ultrasonic vibration (UV)-500, UV-2000, and conventional compression (CC) respectively. The red one represents high-angle grain boundaries, while the green one represents small-angle grain boundaries. (e)–(h) The hardness distribution maps belonging to the surface of as-cast, UV500, UV-2000, and CC respectively. The color scale represents the hardness values. (For interpretation of the references to color in this figure legend, the reader is referred to the web version of this article.)

light green, yellow, and red, representing grain orientation angles between 0 and $6^\circ,\,6\text{--}12^\circ,\,12\text{--}18^\circ,\,18\text{--}24^\circ,\,$ and $24\text{--}30^\circ$ respectively. The inset of Fig. 8c shows the percentage of different colors in the map, the orientation angle between 0 and $6^\circ,\,6\text{--}12^\circ,\,12\text{--}18^\circ,\,18\text{--}24^\circ,\,$ and $24\text{--}30^\circ$ being 12.1 %, 50 %, 34.2 %, 3.7 %, and 0 %, respectively, in the CC sample. The same inset in Fig. 8d shows percentages of 3.3 %, 47.2 %, 10.2 %, 5.6 % and 33.8 %, respectively, in the UAPF sample. From the statistical data, it is evident that the proportion of grain rotations in the UAPF samples is significantly larger, especially for the large rotation angles within the range of $24\text{--}30^\circ$. The value increases from 0 % in the CC samples to 33.8 % in the UAPF samples.

As shown in Fig. 8c, a crystal marked "A" exhibits the internal crystal rotation along the direction of the black arrow, as depicted in Fig. 8e. A slight discrepancy in the Euler angles, not exceeding 5°, is noted in the crystals processed by conventional loading. However, as shown in Fig. 8f, a large-angle rotation along "B" is induced by UV loading. The remarkable observation is that within the FCC-grain interiors, a complex array of multi-angle rotations occurs when subjected to UV loading [38]. This phenomenon plays a pivotal role in accommodating a high density of dislocations and alleviating stress concentrations during the formation of sub-grain boundaries, thereby enhancing the deformability of the samples under cyclic loading. The lower dislocation density indicates

the potential activation of diverse slip systems during UV loading, ultimately leading to lattice deflection within FCC grains. Consequently, while constrained by grain boundaries, the crystals within the grain interiors progressively adjust their orientations to align with favorable positions conducive to plastic deformation [39].

3.6. Analysis of the deformation mechanism between CC and UAPF

Apart from setting input energy as the only independent variable, a trial was conducted by adjusting the amplitude to observe the ultrasonic vibration effects on samples. All samples were processed under 500 J energy of UV but with amplitudes ranging from 10 % to 90 % (the maximum amplitude is 44 μm). The results shown in Fig. S4 indicate that the processing time for 10 % amplitude is 21.2 s, but the strain is only 0.4 %. This shows that, although the processing time is long, the low amplitude is insufficient to cause plastic deformation of the material, meaning that the amplitude at this level does not reach the threshold for dislocation appreciation. While 30 % amplitude reduces the time (6.8 s), the strain (2.78 %) is still minimal. However, the high amplitude (22 μm) seems to reach the critical value for deformation, and the sample begins to undergo significant plastic deformation. Due to the proportional relationship between ultrasonic energy power and the

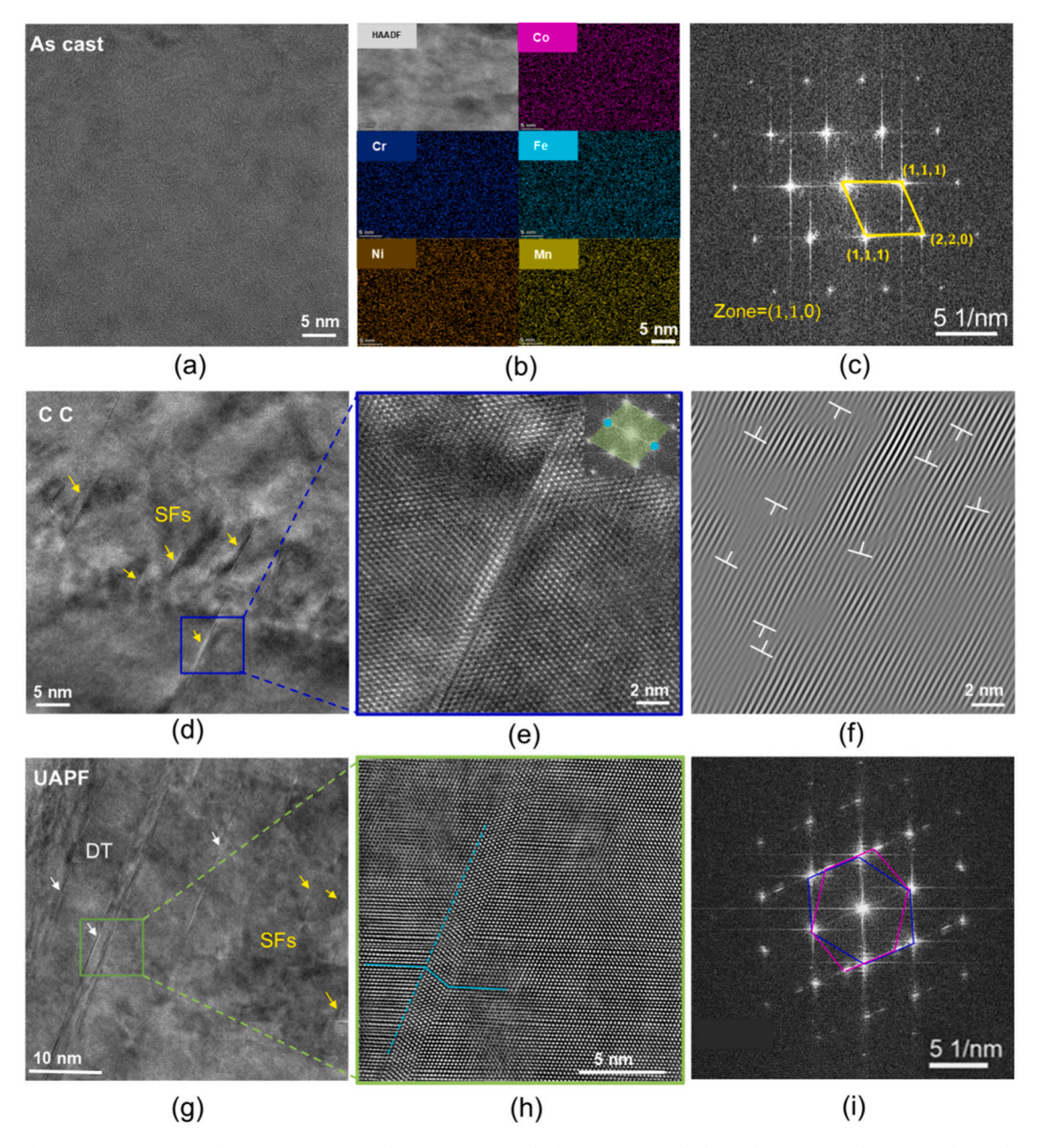


Fig. 7. High-resolution microstructure of as cast, conventional compression, and ultrasonic-assisted plastic forming samples. (a) High-resolution transmission electron microscope (HRTEM) image of the as-cast sample. (b) Elemental distribution maps of the as-cast sample. (c) A selected area electron diffraction (SAED) pattern from (a). (d) HRTEM image of the sample after conventional compression with a strain of 48 %. (e) Enlarged view of stacking faults morphology from the blue frame in (d), inset shows fast Fourier transform of (e). (f) The one-dimensional Fourier-filtered image of (e), the chosen spots were marked blue in the inset of (e), "\(\perpresents \) represents edge dislocations. (g) HRTEM image of the sample after ultrasonic-assisted plastic forming with a strain of 48 %. (h) Enlarged view of deform twinning morphology from the green frame. (i) Fast Fourier transform of (h). (For interpretation of the references to color in this figure legend, the reader is referred to the web version of this article.)

square of amplitude [40], the processing time only costs $1.09 \, s$ at $90 \, \%$ amplitude. This suggests that when the amplitude fails to reach the critical value, no amount of energy is enough to deform the sample. Increasing amplitude and frequency can greatly shorten the processing time, but deformation is ultimately limited by the total input energy.

Fig. 9 shows a schematic distinguishing these two kinds of plastic deformation. From the morphology of the sample, it can be seen that the sample undergoes overall plastic deformation in conventional loading. The strain along the TD direction determines the form quality. However, this ability depends on the Poisson's ratio of the material in conventional loading [41]. In UAPF, due to the more concentrated energy released from the contact surface, the energy gradually decreases as it moves further away from the contact surface; similar phenomena may

also occur near the lower surface contact with the platform. Therefore, after compression, the deformation of the sample is mainly concentrated on the upper and lower surfaces, and its strain in the TD direction is significantly higher than that in CC, which can increase the filling capacity.

The emphasized low-stress processing in UAPF benefits from deformation morphology after compression, degree of dislocation accumulation, grain rotation, and twinning. In convention loading, the defects in the original sample act as dislocation sources, causing dislocation growth under stress. However, due to the large orientation difference between adjacent crystals, they block at grain boundaries [42]. The gradually superimposed dislocations form a stress field at the grain boundaries, forcing the grains to refine into sub-grains to accommodate

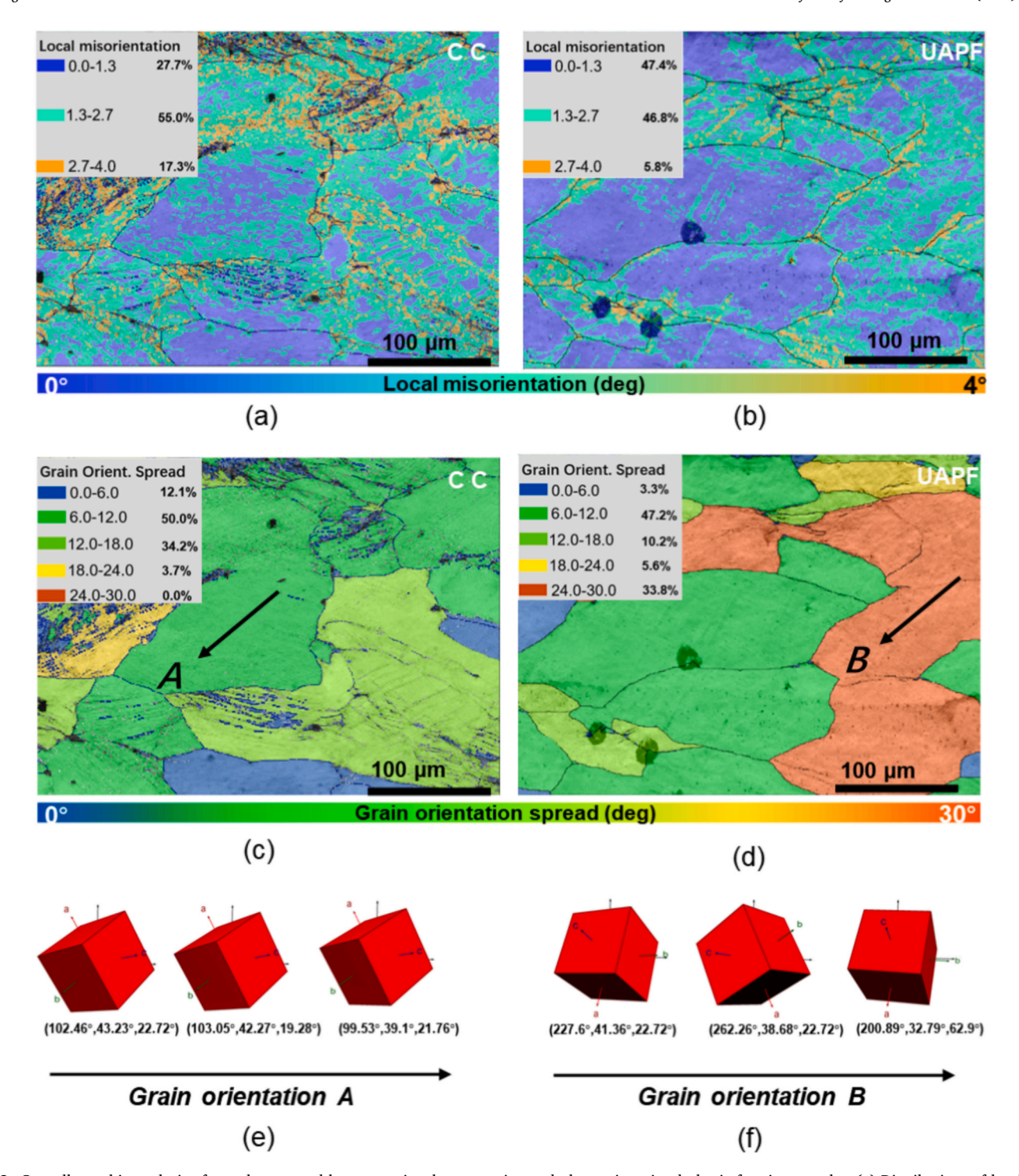


Fig. 8. Crystallographic analysis of sample prepared by conventional compression and ultrasonic-assisted plastic forming samples. (a) Distributions of local misorientations corresponding to geometrically necessary dislocations (GND) in the deformation areas induced by conventional compression (CC). (b) Distributions of local misorientations corresponding to GND in the deformation areas induced by ultrasonic-assisted plastic forming (UAPF). (c) Grain-orientation spread and internal crystal rotation caused by CC. (d) Grain-orientation spread and internal crystal rotation caused by UAPF. (e) Variation of Euler angles in the crystals along orientation B; large angle orientation observed.

more deformations [43].

There is a classic theory of acoustic softening in ultrasonic vibration, which can be explained specifically as the internal structure of crystal materials (dislocations, grain boundaries, etc.) being subjected to ultrasonic vibration, increasing in temperature and energy, providing more energy for the activation of the dislocation slip [44]. This results in a softening phenomenon with reduced deformation load, which is

evident in this research. This acoustic softening enables a different deformation behavior, where a large number of dislocations are accommodated by deformation in the TD direction, resulting in a lower geometric dislocation density in Fig. 8b.

Another factor is the grain rotation in UAPF with higher degrees of freedom due to its dynamic load. The twinning formed is also a manifestation of its adaptive deformation; the grains can extend in the TD

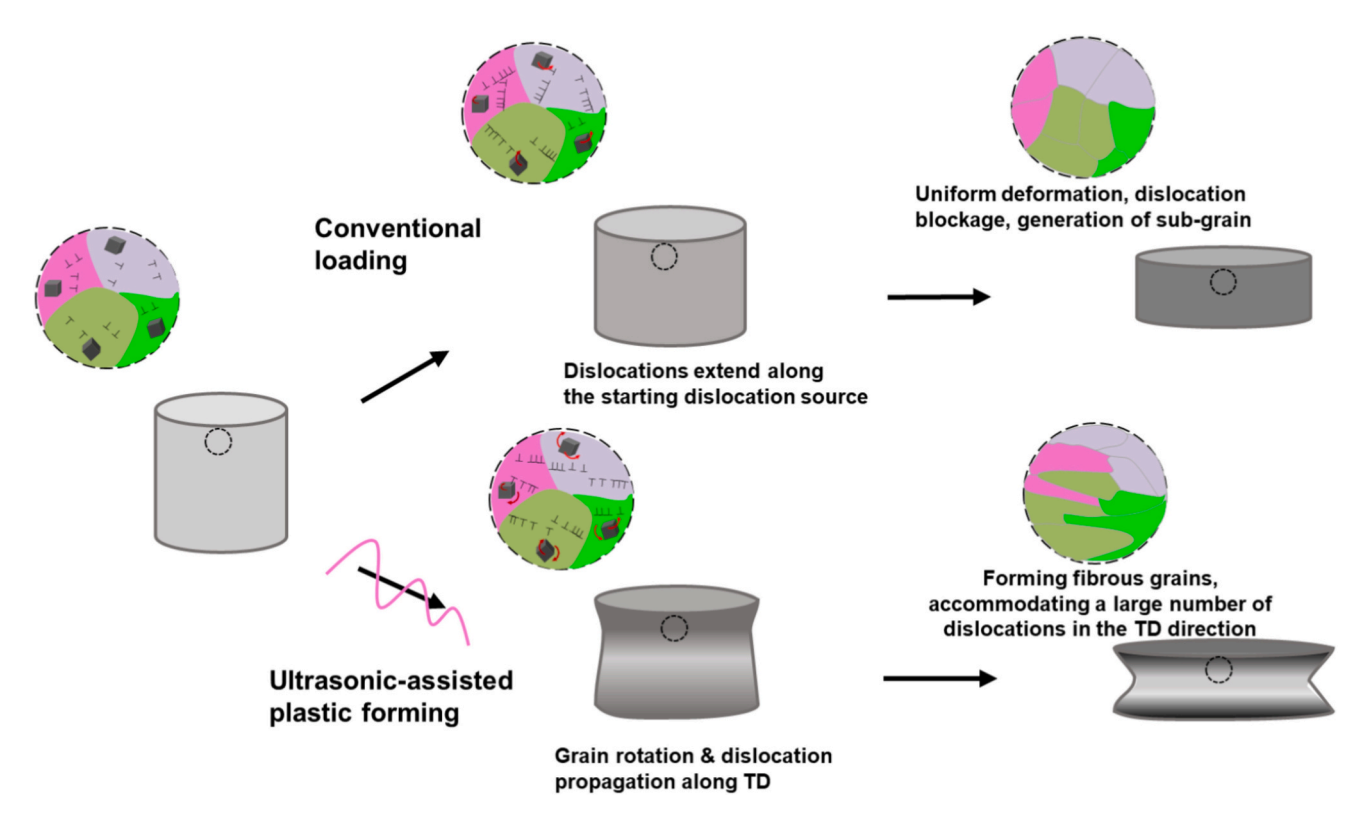


Fig. 9. Schematic of microstructure evolution and deformation mechanisms under different loading.

direction, which can accommodate an increase in deformation volume and greatly reduce the hindrance between grains. Therefore, the grains form a fibrous morphology elongated along TD, as seen in Fig. 6c.

3.7. Display of formed samples

Through this UAPF approach, microscale and nanoscale structures in HEA surface, as well as some parts with special shapes, were successfully obtained under liquid nitrogen in seconds. Fig. 10a is a schematic diagram of the process; the HEA disk was placed on the mold with the designed shape, the horn transmitted force and vibration to the HEA sample, then the sample was deformed plastically quickly and filled the cavity with designed shapes. Fig. 10b shows the HEA with some nanowires, and the diameter of these nanowires is approximately 390 nm, duplicated from an anodic aluminum oxide (AAO) template. These nanostructures have potential applications in the field of photothermal therapy [35]. Fig. 10c shows some straight groove structures on the HEA, duplicated from a stainless steel mold with structures approximately 120 µm wide. In general, the more precise the structure to be machined, the more difficult and time-consuming it is. Thus, it should be emphasized that the advantage of UAPF lies in forming structures with critical dimensions on the surface of HEAs with high efficiency.

Apart from the multi-scale structures mentioned above, Fig. 10d shows a square component, Fig. 10e shows a pentagram component, and Fig. 10f shows an involute gear. During the process, a HEA sample with a diameter of 5 mm was placed on the platform. The shaped molds (the details of the molds were mentioned in the experimental section) were placed on the HEA and in direct contact, and these components were processed in seconds under UV with a good replication rate. Notably, as long as the material possesses good forming ductility, various complex shapes can be replicated. Fig. 10g demonstrates three components with the abbreviation "SZU" on it. Using other technologies, obtaining structures and parts shown in Fig. 10 may require high temperature and difficult processes, such as hot pressing, slow wire cutting, or laser cutting. UAPF shows several advantages, one being forming without any

heating and even under a liquid environment at a low temperature of approximately 77 K. Another advantage is the short forming time, as it typically took hours to fabricate such parts with special shapes by using wire cutting, but UAPF costs only seconds. Furthermore, UAPF has a higher replication ratio than conventional compression forming. Owning to dynamic loading, prepared parts can be assembled and used. Therefore, UAPF is a low-temperature forming technology with significant potential application value.

4. Conclusion

This study suggests that ultrasonic-assisted plastic forming (UAPF) is an efficient method for forming multi-scale structures, and macroscopically functional components under ultra-low temperature conditions. Although a temperature increase of 200–300 K was detected during the processing, it is not sufficient to alter the material's properties. To the application of high-frequency ultrasonic dynamic loading, facilitates a rapid energy release, enabling samples to reach a high strain within 1–5 s, demonstrating the high efficiency of this technique. Moreover, ultrasonic vibration can induce grain refinement, resulting in a notable Vickers hardness increase of 39.1 %, with an effective depth of influence reaching up to 0.5 mm. This highlights dual capability of UAPF to simultaneously form and strengthen materials.

Additionally, UAPF addresses the challenges posed by Portevin-Le Chatelier effect, resulting in smooth and clean surface morphology and enabling a higher replication ratio during the forming process. Notably, achieving the same strain as conventional compression requires only $\sim\!15\,\%$ of the stress in UAPF. This disparity is due to different deformation mechanisms at play in UAPF compared to conventional compression. The efficiency and low forming stress of UAPF make it a highly suitable method for industrial production, particularly in promoting the lightweight of forming equipment. Furthermore, the UAPF process allows for concurrent surface modification during material forming, enhancing its practical utility.

We believe that UAPF has significant potential for engineering

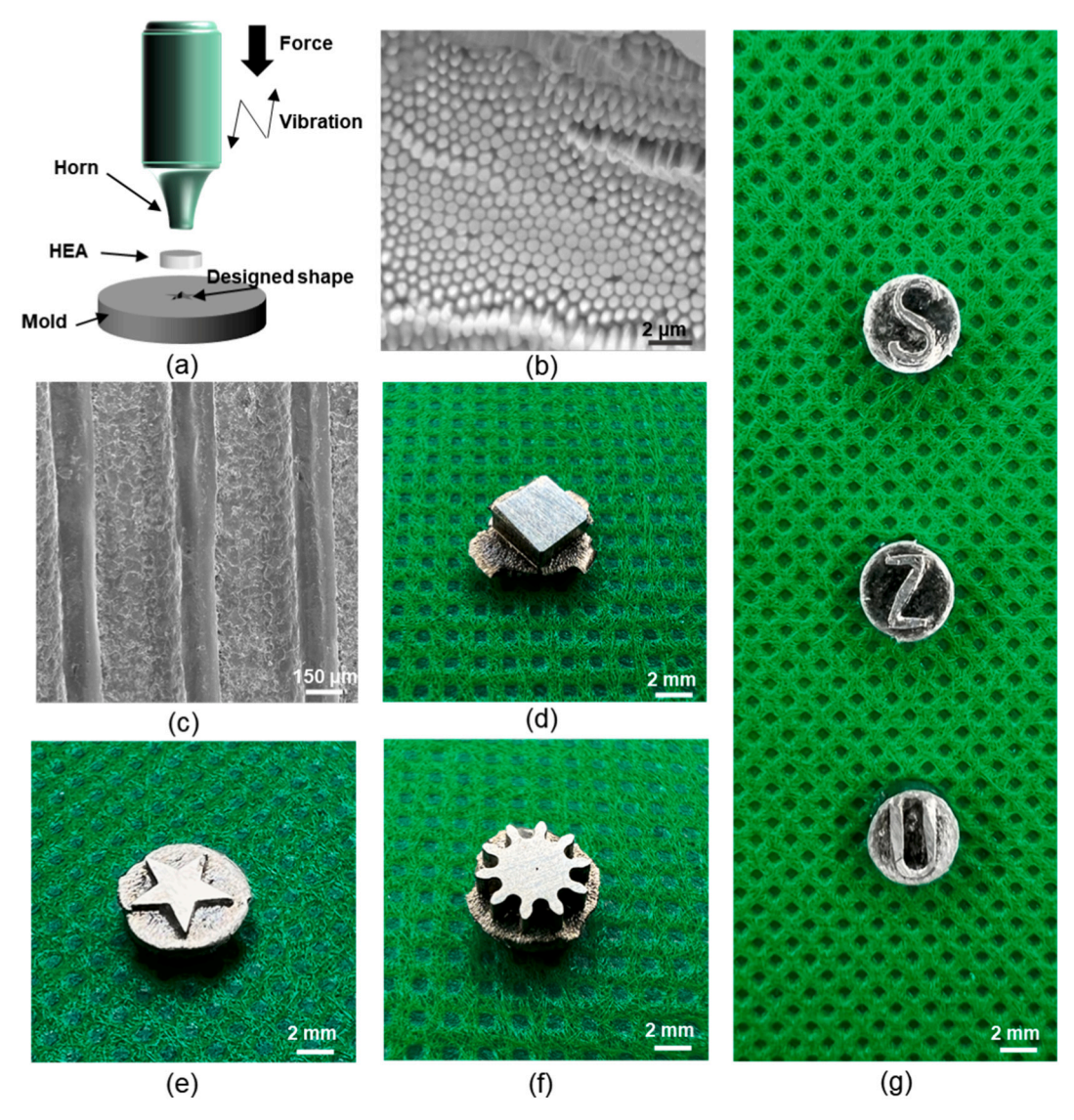


Fig. 10. Display of formed samples and structures by ultrasonic-assisted plastic forming. (a) A schematic diagram of ultrasonic-assisted plastic forming (UAPF) under liquid nitrogen. (b) Scanning electron microscope (SEM) image shows the high-entropy alloy nanowire prepared using an anodic aluminum oxide template of 390 nm. (c) SEM image depicting the replication of a high sample featuring a straight groove structure. (d) A square component made by UAPF. (e) A pentagram component made by UAPF. (f) An involute gear made by UAPF. (g) Three components with the abbreviation "SZU" on it.

applications in forming metal alloys, especially in extreme environments. The proposed forming mechanism reveals a "softening" phenomenon in metallic materials under high-frequency dynamic loading, demonstrating that dynamic forming requires significantly less stress than conventional methods while enhancing material deformability. These findings provide valuable insights into the plastic deformation of metal materials under dynamic loading conditions and serve as a reference for further exploration of advanced forming techniques in extreme environments.

CRediT authorship contribution statement

Yu Zhang: Writing – original draft, Methodology, Investigation, Data curation, Conceptualization. Pengyu Huang: Methodology, Investigation. Luyao Li: Methodology, Data curation. Xin Li: Investigation, Formal analysis. Wenxin Wen: Methodology. Sajad Sohrabi: Writing – review & editing. Jinbiao Huang: Validation, Formal analysis. Wenhao Lu: Software, Formal analysis. Yong Xiao: Writing – review & editing, Supervision, Resources. Dan Li: Formal analysis. Jiang Ma: Writing – review & editing, Supervision, Resources, Funding

acquisition.

Declaration of competing interest

The authors declare that they have no known competing financial interests or personal relationships that could have appeared to influence the work reported in this paper.

Acknowledgments

The work was financially supported by the Key Basic and Applied Research Program of Guangdong Province, China (Grant No. 2019B030302010), the National Key Research and Development Program of China (Grant No. 2018YFA0703605), the NSF of China (Grant No. 52122105, 51971150, 52271150), and the Science and Technology Innovation Commission Shenzhen (Grants No. RCJC20221008092730037, 20220804091920001). The authors also thank the assistance on microscope observation received from the Electron Microscope Center of Shenzhen University.

Appendix A. Supplementary data

Supplementary data to this article can be found online at https://doi.org/10.1016/j.jmapro.2025.01.097.

References

- [1] Eswarappa Prameela S, Pollock TM, Raabe D, Meyers MA, Aitkaliyeva A, Chintersingh K-L, et al. Materials for extreme environments. Nature Reviews Materials 2022;8(2):81–8. https://doi.org/10.1038/s41578-022-00496-z.
- [2] Li J, Li S, Zhang Y, Yang Y, Russi S, Qian G, et al. Multiphase, multiscale chemomechanics at extreme low temperatures: battery electrodes for operation in a wide temperature range. Adv. Energy Mater. 2021;11(37):2102122. https://doi. org/10.1002/aenm.202102122.
- [3] Liu Y, Kreimeier M, Stumpf E, Zhou Y, Liu H. Overview of recent endeavors on personal aerial vehicles: a focus on the US and Europe led research activities. Prog. Aerosp. Sci. 2017;91:53–66. https://doi.org/10.1016/j.paerosci.2017.03.001.
- [4] Richter C, Boschker H, Dietsche W, Fillis-Tsirakis E, Jany R, Loder F, et al. Interface superconductor with gap behaviour like a high-temperature superconductor. Nature 2013;502(7472):528–31. https://doi.org/10.1038/nature12494.
- [5] Li C, Hu H, Yang MF, Pei ZY, Zhou Q, Ren X, et al. Characteristics of the lunar samples returned by the Chang'E-5 mission. Natl. Sci. Rev. 2022;9(2):nwab188. https://doi.org/10.1093/nsr/nwab188.
- [6] Liu J, Yao R, Yu L, Gan X, Wang X. Line design and optimization for polar expedition cruise ships with transoceanic voyage characteristics. J. Mar. Sci. Technol. 2023;28(1):270–87. https://doi.org/10.1007/s00773-023-00924-x.
- [7] Wu X, Gao Y, Wang Y, Fan R, Ali Z, Yu J, et al. Recent developments on epoxy-based syntactic foams for deep sea exploration. J. Mater. Sci. 2020;56(3):2037–76. https://doi.org/10.1007/s10853-020-05420-w.
- [8] Williams JP, Paige DA, Greenhagen BT, Sefton-Nash E. The global surface temperatures of the Moon as measured by the Diviner Lunar Radiometer Experiment. Icarus 2017;283:300–25. https://doi.org/10.1016/j. icarus.2016.08.012.
- [9] Panin VE, Derevyagina LS, Lemeshev NM, Korznikov AV, Panin AV, Kazachenok MS. On the nature of low-temperature brittleness of BCC steels. Phys. Mesomech. 2014;17(2):89–96. https://doi.org/10.1134/S1029959914020015.
- [10] Zhang Y, Chen B, Guan D, Xu M, Ran R, Ni M, et al. Thermal-expansion offset for high-performance fuel cell cathodes. Nature 2021;591(7849):246–51. https://doi. org/10.1038/s41586-021-03264-1.
- [11] Herrmann J, Inden G, Sauthoff G. Deformation behaviour of iron-rich iron-aluminum alloys at low temperatures. Acta Mater. 2003;51(10):2847–57. https://doi.org/10.1016/s1359-6454(03)00089-2.
- [12] Mirzadeh H. High strain rate superplasticity via friction stir processing (FSP): a review. Mater. Sci. Eng. A 2021;819:141499. https://doi.org/10.1016/j. msea.2021.141499.
- [13] Ko YG, Lee CS, Shin DH, Semiatin SL. Low-temperature superplasticity of ultrafine-grained Ti-6Al-4V processed by equal-channel angular pressing. Metall. Mater. Trans. A 2006;37(2):381–91. https://doi.org/10.1007/s11661-006-0008-z.
- [14] Charit I, Mishra RS. Low temperature superplasticity in a friction-stir-processed ultrafine grained Al–Zn–Mg–Sc alloy. Acta Mater. 2005;53(15):4211–23. https://doi.org/10.1016/j.actamat.2005.05.021.
- [15] Otto F, Dlouhý A, Somsen C, Bei H, Eggeler G, George EP. The influences of temperature and microstructure on the tensile properties of a CoCrFeMnNi highentropy alloy. Acta Mater. 2013;61(15):5743–55. https://doi.org/10.1016/j. actamat.2013.06.018.
- [16] Naeem M, He H, Harjo S, Kawasaki T, Lin W, Kai J-J, et al. Temperature-dependent hardening contributions in CrFeCoNi high-entropy alloy. Acta Mater. 2021;221: 117371. https://doi.org/10.1016/j.actamat.2021.117371.
- [17] Naeem M, He H, Zhang F, Huang H, Harjo S, Kawasaki T, et al. Cooperative deformation in high-entropy alloys at ultralow temperatures. Science. Advances 2020;6(13):eaax4002. https://doi.org/10.1126/sciadv.aax4002.
- [18] Fan C, Li L, Wen W, Li H, Fu J, Ruan W, et al. Rapid amorphization of CrMnFeCoNi high-entropy alloy under ultrasonic vibrations. Mater. Des. 2023;225:111575. https://doi.org/10.1016/j.matdes.2022.111575.
- [19] Li X, Li L, Sohrabi S, Fu J n, Li Z, Chen Z, et al. Ultrasonic vibration enabled underliquid forming of metallic glasses. Sci. Bull. 2024;69(2):163–6. https://doi.org/ 10.1016/j.scib.2023.11.049.
- [20] Chen Z, Ren S, Zhao R, Zhu J, Li X, Zhang H, et al. Plasticity and rejuvenation of aged metallic glasses by ultrasonic vibrations. J. Mater. Sci. Technol. 2024;181: 231–9. https://doi.org/10.1016/j.jmst.2023.09.029.
- [21] Ma J, Yang C, Liu X, Shang B, He Q, Li F, et al. Fast surface dynamics enabled cold joining of metallic glasses. Sci. Adv. 2019;5:eaax7256. https://doi.org/10.1126/ sciadv.aax7256.

- [22] Li L, Li X, Huang Z, Huang J, Liu Z, Fu J, et al. Joining of metallic glasses in liquid via ultrasonic vibrations. Nat. Commun. 2023;14(1). https://doi.org/10.1038/ s41467-023-42014-x.
- [23] Li Z, Li X, Huang Z, Zhang Z, Liang X, Liu H, et al. Ultrasonic-vibration-enhanced plasticity of an entropic alloy at room temperature. Acta Mater. 2022;225. https://doi.org/10.1016/j.actamat.2021.117569.
- [24] Wen W-X, Li L-Y, Li Z, Ruan W-Q, Ren S, Zhang Z-X, et al. Ultrasonic vibrationassisted multi-scale plastic forming of high-entropy alloys in milliseconds. Rare Metals 2022;42(4):1146–53. https://doi.org/10.1007/s12598-022-02171-2.
- [25] Guo F-S, Day BM, Chen Y-C, Tong M-L, Mansikkamäki A, Layfield RA. Magnetic hysteresis up to 80 kelvin in a dysprosium metallocene single-molecule magnet. Science 2018;362(6421):1400–3. https://doi.org/10.1126/science.aav0652.
- [26] Owen LR, Pickering EJ, Playford HY, Stone HJ, Tucker MG, Jones NG. An assessment of the lattice strain in the CrMnFeCoNi high-entropy alloy. Acta Mater. 2017;122:11–8. https://doi.org/10.1016/j.actamat.2016.09.032.
- [27] Zhang X, Yu H, Li C. Microstructure and mechanical properties of 2A10 aluminum alloy bar subjected to dynamic heading. J. Mater. Process. Technol. 2016;227: 259–67. https://doi.org/10.1016/j.jmatprotec.2015.09.001.
- [28] Rowlands BS, Rae C, Galindo-Nava E. The Portevin-Le Chatelier effect in nickel-base superalloys: origins, consequences and comparison to strain ageing in other alloy systems. Prog. Mater. Sci. 2023;132:101038. https://doi.org/10.1016/j.pmatsci.2022.101038.
- [29] Halim H, Wilkinson D, Niewczas M. The Portevin–Le Chatelier (PLC) effect and shear band formation in an AA5754 alloy. Acta Mater. 2007;55(12):4151–60. https://doi.org/10.1016/j.actamat.2007.03.007.
- [30] Yuzbekova D, Mogucheva A, Zhemchuzhnikova D, Lebedkina T, Lebyodkin M, Kaibyshev R. Effect of microstructure on continuous propagation of the Portevin–Le Chatelier deformation bands. Int. J. Plast. 2017;96:210–26. https://doi.org/10.1016/j.ijplas.2017.05.004.
- [31] Langenecker B. Effects of Ultrasound on Deformation Characteristics of Metals. IEEE Transactions on Sonics and Ultrasonics 1966;13(1):1–8. https://doi.org/ 10.1109/T-SU.1966.29367.
- [32] Scholz-Reiter B, Weimer D, Thamer H. Automated surface inspection of cold-formed micro-parts. CIRP Ann. 2012;61(1):531–4. https://doi.org/10.1016/j.cirp.2012.03.131.
- [33] Zhao W, Han J-K, Kuzminova YO, Evlashin SA, Zhilyaev AP, Pesin AM, et al. Significance of grain refinement on micro-mechanical properties and structures of additively-manufactured CoCrFeNi high-entropy alloy. Mater. Sci. Eng. A 2021; 807:140898. https://doi.org/10.1016/j.msea.2021.140898.
- [34] Chen L, Cao T, Wei R, Tang K, Xin C, Jiang F, et al. Gradient structure design to strengthen carbon interstitial Fe40Mn40Co10Cr10 high entropy alloys. Mater. Sci. Eng. A 2020:772:138661. https://doi.org/10.1016/j.msea.2019.138661.
- [35] Shahmir H, Mehranpour MS, Arsalan Shams SA, Langdon TG. Twenty years of the CoCrFeNiMn high-entropy alloy: achieving exceptional mechanical properties through microstructure engineering. Journal of Materials Research and Technology 2023;23:3362–423. https://doi.org/10.1016/j.jmrt.2023.01.181.
- [36] Wang B, Wang C, Liu B, Zhang X. Dynamic mechanical properties and microstructure of an (Al0.5CoCrFeNi)0.95Mo0.025C0.025 high entropy alloy. Entropy 2019;21(12):1154. https://doi.org/10.3390/e21121154.
- [37] Han CS, Gao H, Huang Y, Nix WD. Mechanism-based strain gradient plasticity—I. Theory. Journal of the Mechanics & Physics of Solids 1999;47(5):1239–63. https://doi.org/10.1016/S0022-5096(98)00103-3.
- [38] Zhu Q, Cao G, Wang J, Deng C, Li J, Zhang Z, et al. In situ atomistic observation of disconnection-mediated grain boundary migration. Nat. Commun. 2019;10(1):156. https://doi.org/10.1038/s41467-018-08031-x.
- [39] Mishra S, Suresh M, More AM, Bisht A, Nayan N, Suwas S. Texture control to reduce yield strength anisotropy in the third generation aluminum-copper-lithium alloy: experiments and modeling. Mater. Sci. Eng. A 2021;799:140047. https://doi. org/10.1016/j.msea.2020.140047.
- [40] Lu X, Shen H, Zhao K, Wang Z, Peng H, Liu W. Micro-/nanomachines driven by ultrasonic power sources. Chem. Asian J. 2019;14(14):2406–16. https://doi.org/ 10.1002/asia.201900281.
- [41] Saxena KK, Das R, Calius EP. Three decades of auxetics research materials with negative Poisson's ratio: a review. Adv. Eng. Mater. 2016;18(11):1847–70. https://doi.org/10.1002/adem.201600053.
- [42] Gao P, Sun S, Li H, Niu R, Han S, Zong H, et al. Ultra-strong and thermally stable nanocrystalline CrCoNi alloy. J. Mater. Sci. Technol. 2022;106:1–9. https://doi. org/10.1016/j.jmst.2021.08.009.
- [43] Laktionova MA, Tabchnikova ED, Tang Z, Liaw PK. Mechanical properties of the high-entropy alloy Ag0.5CoCrCuFeNi at temperatures of 4.2–300 K. Low Temperature Physics 2013;39(7):630–2. https://doi.org/10.1063/1.4813688.
- [44] Zhao Y, Zhai J, Guan Y, Chen F, Liu Y, Li Y, et al. Molecular dynamics study of acoustic softening effect in ultrasonic vibration assisted tension of monocrystalline/polycrystalline coppers. J. Mater. Process. Technol. 2022;307: 117666. https://doi.org/10.1016/j.jmatprotec.2022.117666.